Fukasawa *et al. Earth, Planets and Space* (2024) 76:38
https://doi.org/10.1186/s40623-024-01977-x

Earth, Planets and Space

FULL PAPER

Open Access

Impedance of electric field sensors in magnetized plasmas: particle-in-cell simulations

Ibuki Fukasawa[1], Yohei Miyake[2], Hideyuki Usui[2], Koshiro Kusachi[2], Satoshi Kurita[3] and Hirotsugu Kojima[3*]

Abstract

To obtain both the intensities and phases of electric fields, it is necessary to calibrate the data observed by the sensor by consulting the sensor characteristics. The frequency profile of the sensor impedance obtained from the simulation is roughly consistent with that obtained from the theory. However, some differences are identified in the frequency profile of the sensor impedance obtained from the simulation compared to the theory. We conducted simulations using the particle-in-cell (PIC) simulation tool to analyze the impedance of electric field sensors immersed in magnetized space plasmas. The simulation model comprised a dipole sensor placed in a three-dimensional simulation box filled with electrons and ions. The dipole sensor was represented by perfect conductor rods. We carefully selected simulation parameters and employed an appropriate feeding technique to accurately evaluate the sensor impedance. We observed significant changes in the frequency dependence of the sensor impedance as cyclotron frequency varied. To understand the simulation results, we introduced the linear dispersion relation. By comparing the real part of the sensor impedance with the $\omega - k$ diagram, we found that the impedance peaks corresponded to frequencies at which branches of plasma waves were present, with $k = k_{\mathrm{half}}$, representing half the wavelength equal to the tip-to-tip sensor length, i.e., the sensor can be assumed as the half-wavelength dipole antenna.

Keywords Particle-in-cell simulation, Sensor impedance, Plasma waves, Electric field sensors

*Correspondence:
Hirotsugu Kojima
kojima.hirotsugu.6m@kyoto-u.ac.jp
Full list of author information is available at the end of the article

Graphical Abstract

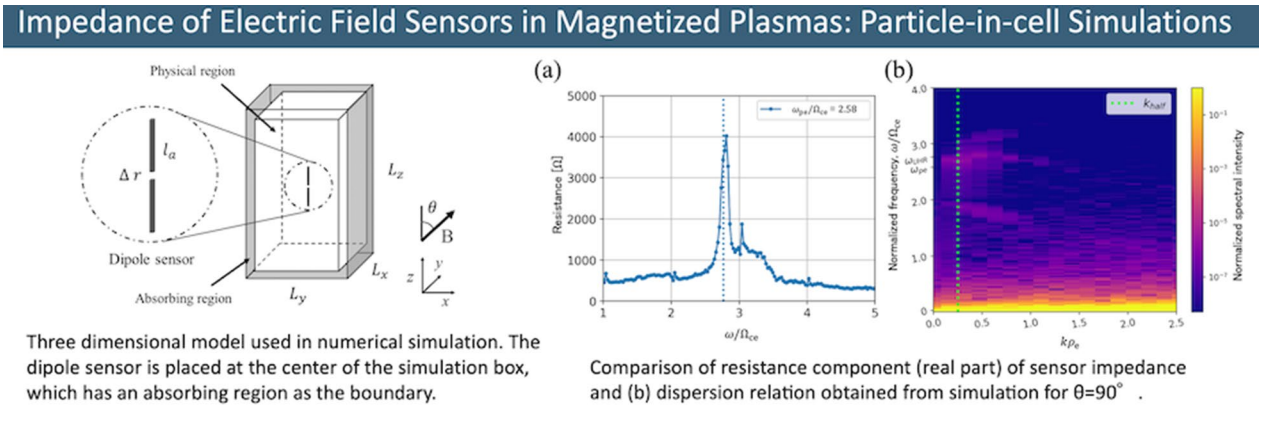

Introduction

Accurate measurement and a quantitative understanding of space environments are essential for future space utilization and development. Since space plasmas are collisionless, plasma waves transport the energies and momentums of plasma particles. Plasma wave observations are thus indispensable for space missions that explore space environments. Dipole sensors installed on scientific spacecraft are commonly used for observing the electric field components of plasma waves (Barrington and Belrose 1963). To obtain both the intensities and phases of electric fields, it is necessary to calibrate the data picked up by the electric field sensor. However, the electric field sensors in plasmas exhibit complicated properties because plasma is a dispersive medium. In particular, the impedance and

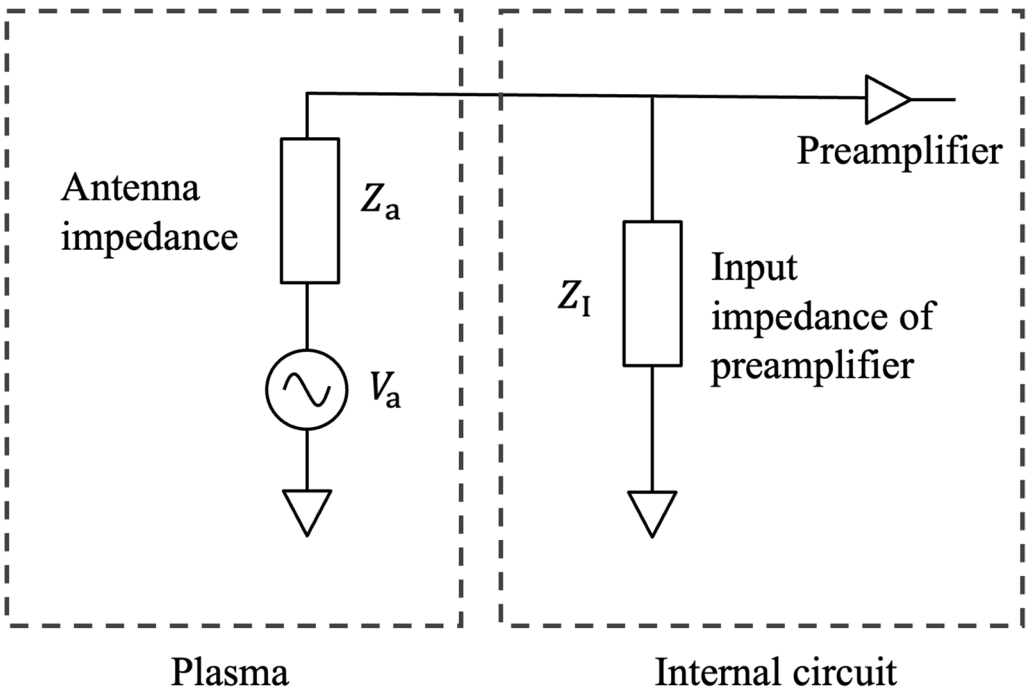

Fig. 1 Equivalent front-end circuit for electric field measurement system. V_a is the voltage induced by the applied electric field, Z_a the sensor impedance, and Z_I the input impedance at the base of the sensor

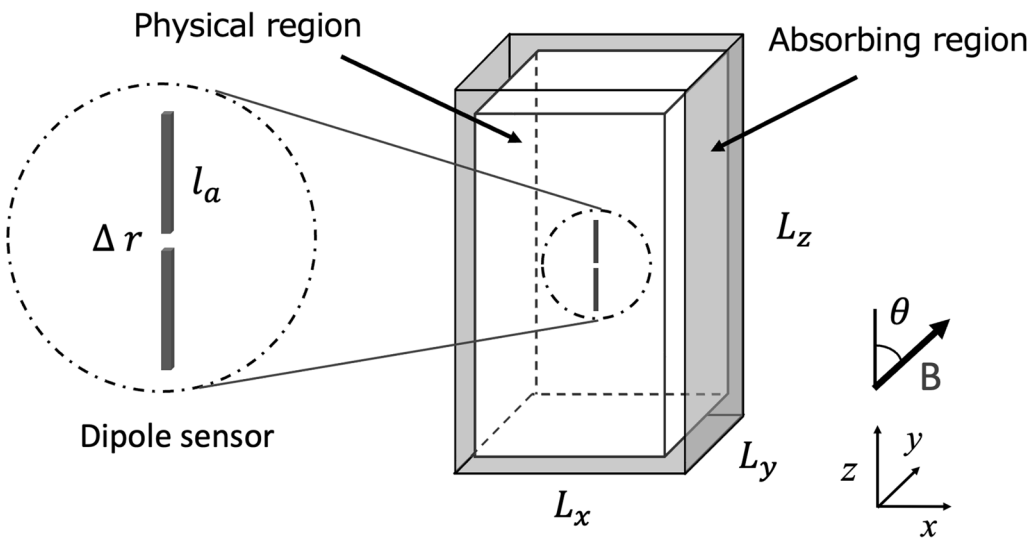

Fig. 2 Three dimensional model used in numerical simulation. The dipole sensor is placed at the center of the simulation box, which has an absorbing region as the boundary

effective length of a sensor immersed in space plasmas are very sensitive to the parameters, such as temperature and density, of the surrounding plasma (Stix 1992). In this study, we examine the impedance of electric field sensors aboard satellites in space plasmas.

Figure 1 shows a simplified equivalent front-end circuit for an electric field sensor and the input of its preamplifier. V_a is the voltage induced by electric fields, Z_a is the sensor impedance, and Z_I is the input impedance of the pick up circuit such as preamplifiers. As shown in Fig. 1, the voltage observed by the electric field sensor is divided into the sensor impedance and the input impedance.

The sensor impedance is complex, so the calibration of the phase and absolute value of observed plasma waves should be performed under consideration of the sensor impedance as well as the input impedance of the preamplifier. Hence, a quantitative understanding of the characteristics of the sensor impedance is required for the precise characterization of observed electric fields.

The impedance of electric field sensors in plasmas has been studied mainly using analytical approaches and numerical calculations based on simplified models (e.g. Balmain 1964; Schiff and Fejer 1970; Meyer and Vernet 1974). However, these studies adopt the assumption of simple current profiles induced on sensor elements. That is, they did not take into account the actual current profiles, which strongly depend on the relative sensor element lengths and the wavelengths of observed plasmas. Consideration of plasma kinetic effects is also important in a discussion of the effects of the plasma sheath that forms around sensors.

In parallel with theoretical studies, in situ measurements of the impedance of a sensor in space plasmas have been conducted by scientific satellites (e.g. Hashimoto et al. 1991; Matsuda et al. 2021) and rockets (e.g. Wakabayashi and One 2006). An analysis of the measurement data showed that the impedance of electric field sensors in space plasmas can be represented by an equivalent electric circuit that consists of a resistance and a capacitance connected in parallel (Tsutsui et al. 1997).

Although past theoretical and experimental studies have contributed to the understanding of the fundamental behavior of electric field sensors immersed in plasmas, it is difficult to apply conventional methods to realistic models because the characteristics of electric field sensors are influenced by satellite structures and the relative sensor element lengths and plasma wave lengths.

Simulation studies have potential to overcome the limitations of theoretical and experimental studies. They can deal with realistic models that consider factors such as inhomogeneities, kinetics, and satellite structures.

Various numerical approaches can be applied to study the characteristics of electric field sensors in plasmas (Luebbers et al. 1991; Spencer et al. 2008). Among them, the particle-in-cell (PIC) method (Birdsall and Langdon 2018) has been applied to simulations that deal with the kinetic effects of particles (Usui et al. 2004; Miyake et al. 2008).

In this study, we show the simulation results obtained using the PIC approach and discuss the sensor impedance calculated for the various values of the magnetic

field intensity and relative angle between the sensor and the background magnetic field.

PIC simulation tool for analysis of electric field sensors

Simulation model

The present study uses the ElectroMagnetic Spacecraft Environment Simulator (EMSES) (Miyake and Usui 2009). In this code, both electrons and ions are modeled as a large number of charged "superparticles (Matsumoto and Omura 1993)." The algorithms used in the plasma particle and electromagnetic field solvers are based on the standard explicit full PIC method.

The most important feature of the EMSES is that it can deal with structures inside a simulation box as inner boundaries. We place an ideal conductor rod that is equivalent to an element of the electric field sensor in the simulation space.

The simulation model is shown in Fig. 2. We place a dipole sensor in the center of a three-dimensional simulation box. We define half the dipole sensor length as l_a. The simulation box is uniformly filled with electrons and ions with finite temperatures in the initial stage. The uniform and stationary magnetic field lies in the y–z plane, and the angle between the sensor and the magnetic field is defined as θ.

The focus in the present paper is the sensor impedance in the frequency range around upper hybrid resonance (UHR) frequency, which is expressed as

$$\Omega_{\mathrm{UHR}} = \sqrt{\omega_{\mathrm{pe}}^2 + \Omega_{\mathrm{ce}}^2}, \tag{1}$$

where ω_{pe} and Ω_{ce} are the plasma frequency and electron cyclotron frequency, respectively. At these frequencies, the motion of ions has little effect on the sensor impedance. However, the ion dynamics cannot be disregarded when considering the steady-state sheath profile around the sensor. Electron–proton plasma is used in the simulation, where the real mass ratio of the proton to the electron (i.e., 1836) is adopted. To realize an isolated system, the boundary condition of the simulation box should be selected appropriately. Different types of boundary conditions are set for the electrostatic (ES) and electromagnetic (EM) fields. When Poisson's equation is applied for the ES component, an open boundary condition is used. For the EM component, we set a field absorbing region using the masking method (Tajima and Lee 1981). The region consists of eight grids from the boundaries of the box to avoid the reflection of EM fields at the boundaries. For particles, a periodic boundary condition is adopted to conserve the number of particles in the simulation box.

Simulation model of sensor elements

The EMSES code treats the objects placed in the simulation box as inner boundaries. In this paper, the sensor bodies are assumed to be perfect conductors. The electric field inside a sensor body and its tangential component to the sensor surface should be zero according to the boundary conditions. As shown in Fig. 2, a sensor placed in the simulation box consists of two conductor rods, with a feeding point between the rods.

To obtain the sensor impedance, the delta-gap feeding technique (Hunsberger et al. 1992) is applied. To obtain the sensor impedance over a wide frequency range in a single run of the simulation, we utilized the following Gaussian voltage pulse:

$$V_{\mathrm{in}} = V_a \frac{d}{dt}\left[\left(\frac{t}{T}\right)^4 \exp\left(-\frac{t}{T}\right)\right], \tag{2}$$

where t is the time and V_a and T characterize the pulse height and width, respectively. The dominant spectral power of the pulse appears at the frequency $\omega_d = 0.152 \times 2\pi/T$. To obtain the impedance of the sensor, the current at the sensor feeding point I_{in} needs to be evaluated. I_{in} is calculated by applying Ampere's law around the feeding point as follows:

$$I_{\mathrm{in}} = \left[\left(B_x^{\mathrm{lower}} - B_x^{\mathrm{upper}}\right)\Delta x + \left(B_y^{\mathrm{right}} - B_y^{\mathrm{left}}\right)\Delta y\right]\frac{\Delta r}{\mu_0}, \tag{3}$$

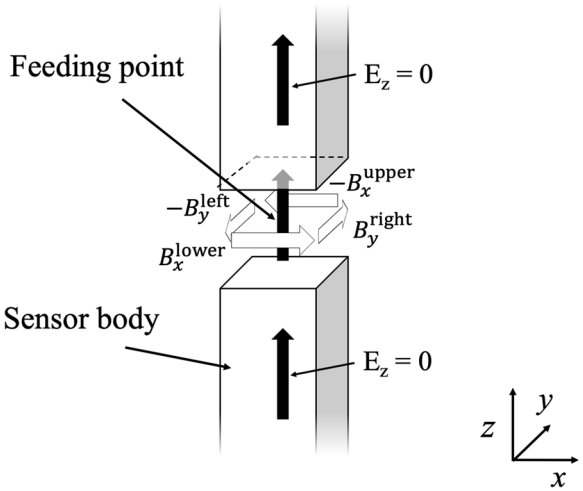

Fig. 3 Field assignment at sensor feeding point. The input voltage $V_{\mathrm{in},z}$ and current I_{in} were calculated from the value at the feeding point

where $\left(\left(B_x^{\text{lower}} - B_x^{\text{upper}}\right) + \left(B_y^{\text{right}} - B_y^{\text{left}}\right)\right)$ is the rotation of the magnetic fields which are defined at grids adjacent to the feeding point, as shown in Fig. 3.

The V_{in} and I_{in} obtained in the time domain are converted to the frequency domain using the discrete Fourier transform. The sensor impedance $Z_{\text{in}}(\omega)$ is calculated as

$$Z_{\text{in}}(\omega) = \frac{V_{\text{in}}(\omega)}{I_{\text{in}}(\omega)}, \tag{4}$$

where $V_{\text{in}}(\omega)$ and $I_{\text{in}}(\omega)$ are the voltage and current at the feeding point in the frequency domain, respectively.

Note that the surface current on the sensor element is obtained by applying Ampere's law around the sensor body. The profile of the magnetic field around the sensor body is self-consistently solved such that the electric field satisfies the appropriate boundary conditions of the sensors as described above. We can evaluate the sensor impedance without any assumptions about the current distribution on the sensor surface.

Table 1 Simulation parameters used for analysis of sensor impedance

Parameter	Symbol	Value
System		
Grid spacing	Δr	$0.031 c\omega_{\text{pe}}^{-1}$
Time step	Δt	$0.016\,\omega_{\text{pe}}^{-1}$
System Length	L_x, L_y, L_z	64 λ_D, 64 λ_D, 128 λ_D
Number of superparticles (electron)		1024/cell
Number of superparticles (ion)		256/cell
Dipole sensor		
Sensor half-length	l_a	$16\lambda_D$
Sensor width in *x* and *y* directions		$1.0\lambda_D$
Delta *r* for feeding point	Δr_{sensor}	$1.0\lambda_D$
Background plasma electrons		
Plasma frequency	ω_{pe}	$2.58\Omega_{\text{ce}}$, $2.93\Omega_{\text{ce}}$, $3.23\Omega_{\text{ce}}$
Thermal velocity	v_{the}	$0.032c$
Mass ratio of proton to electron	m_i/m_e	1836

The values are given in the normalized unit system used in the EMSES

Common parameters in analysis

Table 1 lists the common parameters used in the present simulations. The values are given in the normalized unit system of the EMSES. The grid spacing is $\Delta r = 0.031 c\omega_{\text{pe}}^{-1}$, where c is the speed of light. The simulations ran for a total of 40, 000 steps with $\Delta t = 0.016\omega_{\text{pe}}^{-1}$. The calculated impedance value has the unit Ω. In the present analysis, we set a simulation box with 64, 64, and 128 grids in the x, y, and z directions, respectively.

Sensor impedance in magnetized plasmas

Parametric dependence of sensor impedance

To investigate the parametric dependence of sensor impedance in magnetized plasmas, we varied the values of the parameters Ω_{ce} and θ in the simulations, where θ is the angle between the sensor axis and the background magnetic field. We ran the simulations with plasma frequencies

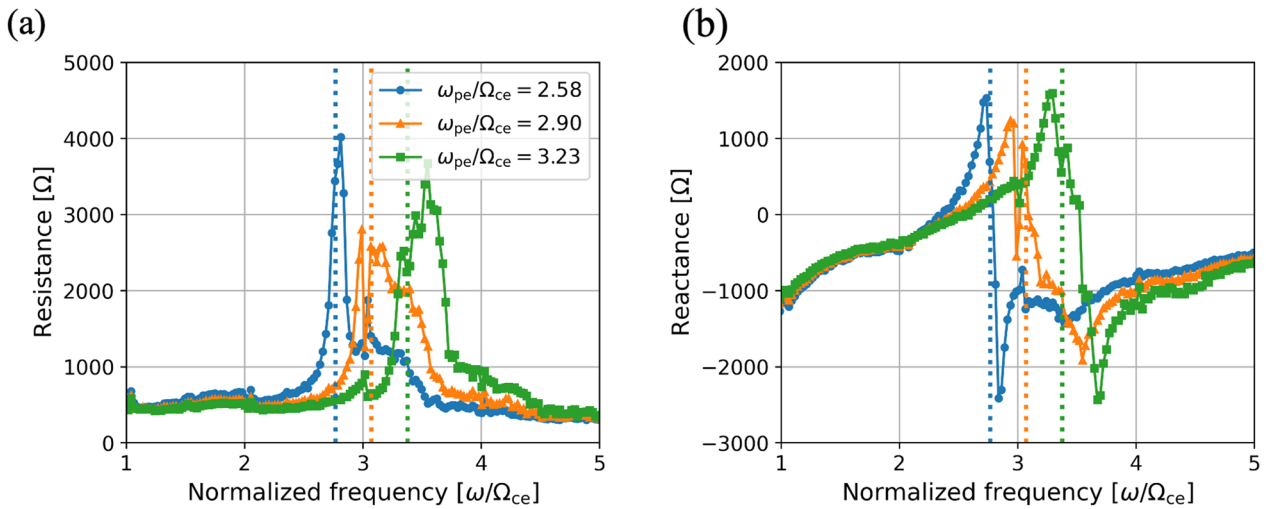

Fig. 4 Dependence of sensor impedance on plasma frequency for $\omega_{\text{pe}}/\Omega_{\text{ce}} = 2.58$, 2.90, and 3.23 with $\theta = 90°$. In panel **a** of the figure, the real component of the sensor impedance is depicted on the left-hand side, whereas panel **b** illustrates the imaginary component on the right-hand side. The vertical dotted lines represent the UHR frequency corresponding to each case

of $\omega_{pe}/\Omega_{ce} = 2.58$, 2.90, and 3.23 with $\theta = 90°$. The other parameters were the same as those listed in Table 1.

The results are shown in Fig. 4. Figure 4a and b respectively shows the frequency dependence of the resistance and reactance components, which are the real and imaginary parts of the calculated impedance, respectively. The vertical dotted lines represent the UHR frequencies corresponding to each case. As shown in Fig. 4a, the resistances in all cases show resonance features with peaks near $\omega/\Omega_{ce} = \Omega_{UHR}$. Another small peak appears near $\omega/\Omega_{ce} = 3.0$. This feature can be seen more clearly in the imaginary part of the sensor impedance(Fig. 4b).

We investigated the dependence of the sensor impedance on the angle θ. $\theta = 0°$ and 90° correspond to simulations in which the sensor is parallel and perpendicular to the magnetic field, respectively. Figure 5 shows the simulation results for $\theta = 0°$, 30°, and 90°. We set the values of the parameters $\omega_{pe}/\Omega_{ce} = 2.58$. The most important feature in Fig. 5 is that the impedance resonance at the second and third harmonics of the cyclotron frequency does not appear at $\theta = 0°$. This result indicates that the impedance peaks at $\omega/\Omega_{ce} \simeq 2$ or 3 are related to the angle between the sensor and the magnetic field. The frequency at the impedance resonance does not show a significant difference among the simulations with different θ values.

Relation between plasma dispersion and sensor impedance

The simulation results in the previous section indicate that the sensor impedance strongly depends on the amplitude of the background magnetic field. This dependence arises from the dispersive nature of magnetized plasmas. In this section, the linear dispersion relation is introduced to understand the simulation results.

Interpretation of simulation results based on linear dispersion

Figure 6a and c shows the $\omega - k$ spectrum plots calculated from the spatial and temporal variations of electric fields observed in the simulations for $\Theta = 90°$ and 0°, respectively. Here, Θ is the wave normal angle relative to the background magnetic field in the Kyoto University Plasma Dispersion Analysis Package (KUPDAP). The color represents the intensity of the electric field in the z direction in the coordinate frame shown in Fig. 2. These $\omega - k$ plots are calculated by the space-time Fourier transform of E_z, the electric field parallel to the sensor, from grid points that do not include the sensor.

The spectral intensity is normalized using the intensity of the Gaussian pulse given in eq. (2) at each frequency. The horizontal and vertical axes are normalized by Ω_{ce} and ρ_e, respectively. Here, ρ_e is the Larmor radius of electrons. For comparison, $\omega - k$ diagrams for $\Theta = 90°$ and $\Theta = 0°$ from the linear dispersion relation are shown in Fig. 6b and d, respectively. These diagrams were computed using the same parameters as those used in each simulation. The dispersion relation of magnetized plasma is numerically solved using the dispersion numerical solver KUPDAP (Sugiyama et al. 2015). KUPDAP takes into account multicomponent, uniform, and collisionless plasmas in a uniform magnetic field. Figure 6b and d shows the real parts of the complex solutions obtained using the plasma parameters listed in Table 1 for $\Theta = 90°$ and $\Theta = 0°$, respectively.

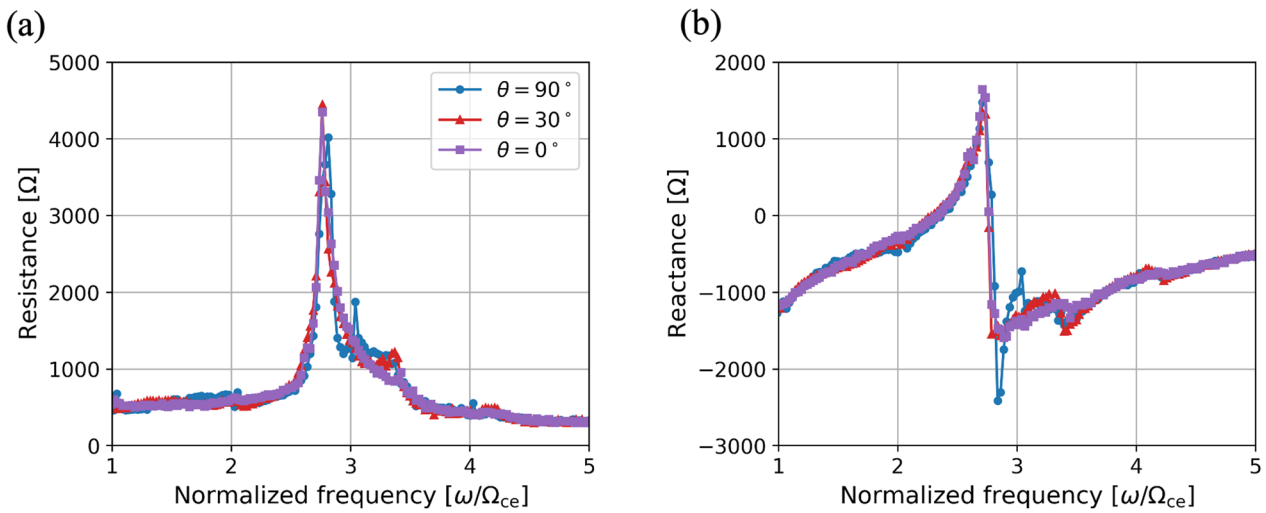

Fig. 5 Dependence of sensor impedance on the θ for three cases with $\theta = 0°$, 30° and 90°. We set the values of the parameters $\omega_{pe}/\Omega_{ce} = 2.58$. **a** Real and **b** imaginary parts of sensor impedance

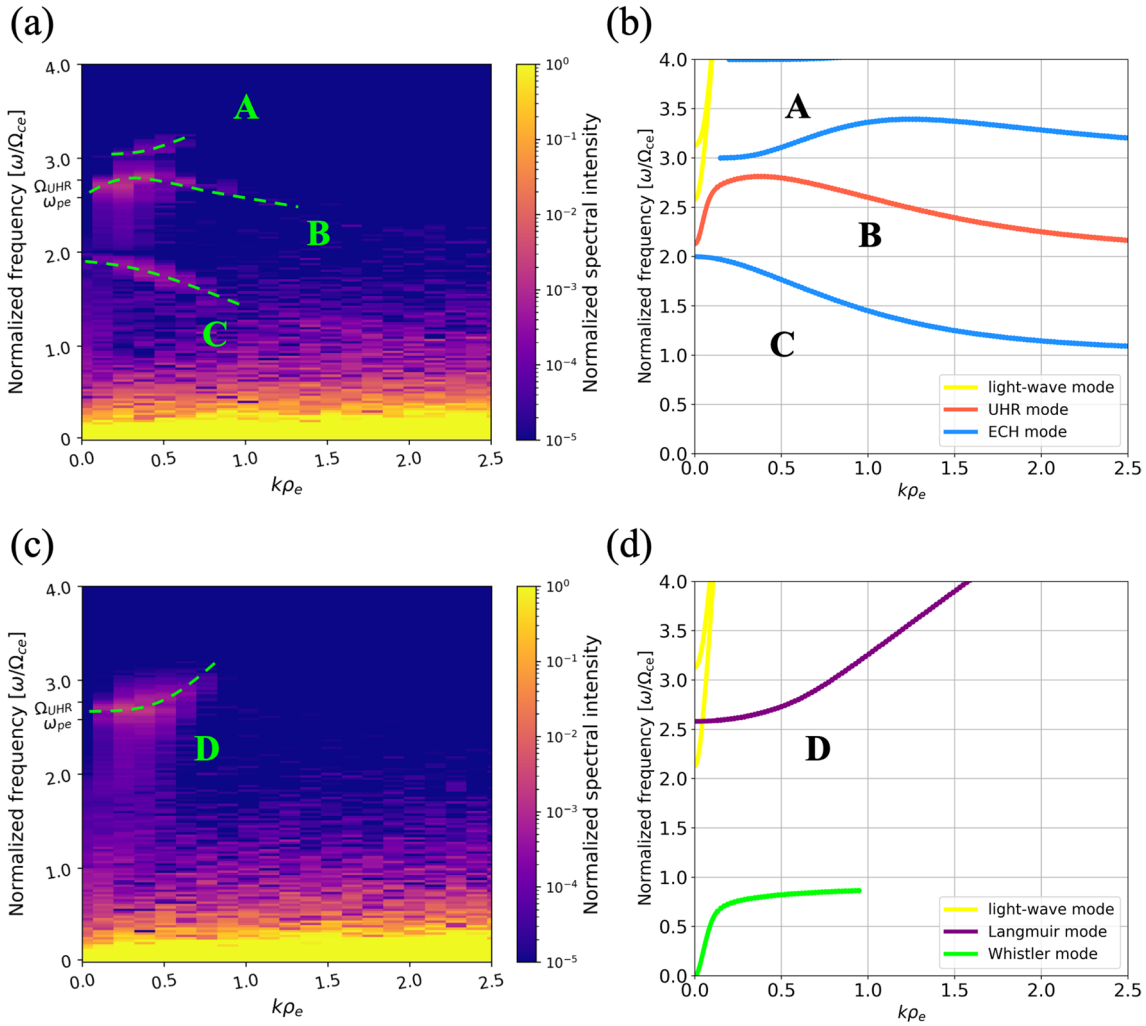

Fig. 6 Dispersion relation obtained from the simulation (left) and KUPDAP (right). For (**a**, **b**) Θ=90◦ and (**c**), (**d**)Θ=0◦. The UHR and ECH modes appear in the ω–k plots in (**a**) and the Langmuir mode appears in the ω–kplots in (**c**) $\Theta = 90°$ and **c**, **b** $\Theta = 0°$. The UHR and ECH modes appear in the $\omega - k$ plots in (**a**) and the Langmuir mode appears in the $\omega - k$ plots in (**c**)

Figure 6 (b) and (d) shows that there are several modes of plasma waves with different properties for $\Theta = 0°$ and 90°.

For $\Theta = 90°$, harmonic structures appear as shown in Fig. 6b. These are the so-called electrostatic electron cyclotron harmonic (ECH) modes, also known as the Bernstein modes (Bernstein 1958). One of those is the UHR mode. The mode connects to the slow X mode, which is an electromagnetic mode near the UHR frequency.

The dispersion relations in Fig. 6b and d are superimposed in Fig. 6a and c, respectively. Figure 6a and b shows good agreement for $k\rho_e < 1$. In particular, the UHR mode denoted as B in Fig. 6a and b, asymptotically approaches Ω_{UHR} in the region of small wavenumber k, leading to the ECH mode, which is consistent with the calculation results. For the ECH mode, denoted as A and C in Fig. 6(a) and (b), the third harmonic branch has intensities at small wavenumber values.

Although there are many similarities between the two diagrams, there are also some differences.

For example, there are no plasma waves in the region of $k\rho_e > 1$ in Fig. 6a, which is due to the ECH waves in this region being subjected to strong cyclotron damping.

Despite the differences, the $\omega - k$ plots from the simulation are mostly consistent with that from KUPDAP for $k\rho_e < 1$ for $\theta = 90°$. Next, we compare the dispersion relation diagram obtained from KUPDAP with that obtained from the simulation for $\theta = 0°$. The results are shown in Fig. 6c and d. The two diagrams in these figures agree for $k\rho_e < 1$. In the simulation results, the Langmuir wave mode appears at a slightly higher frequency than

that calculated by KUPDAP. In addition, the features that appear at $\theta = 90°$, such as the absence of plasma wave modes at $k\rho_e > 1$, the broadening of the branch, and the absence of light-wave modes, can also be observed.

$\omega - k$ diagram obtained from simulation and its relation to sensor impedance

We now discuss the features of sensor impedance obtained in the simulations shown in Fig. 5, with reference to the dispersion relation obtained with the dispersion solver.

Using the parameters, $\omega_{pe}/\Omega_{ce} = 2.58$ and $\theta = 90°$, we explain the relationship between the frequency profile of the sensor impedance and electric field amplitude in the $\omega - k$ space. Figure 7a and b respectively shows the real part of the sensor impedance and the $\omega - k$ diagram calculated from the same simulation. In Fig. 7b, the dotted line indicates the wavenumber k_{half} that corresponds to half the wavelength equal to the tip-to-tip sensor length (i.e., the sensor can be assumed to be a half-wavelength dipole antenna).

From the real part of the sensor impedance and the $\omega - k$ diagram obtained from the simulation, the impedance peaks appear at the frequencies where the UHR and ECH branches are at $k = k_{\mathrm{half}}$. This relation was confirmed in the other simulation cases.

In a vacuum, the frequency that corresponds to the wavelength for which the sensor can be regarded as a

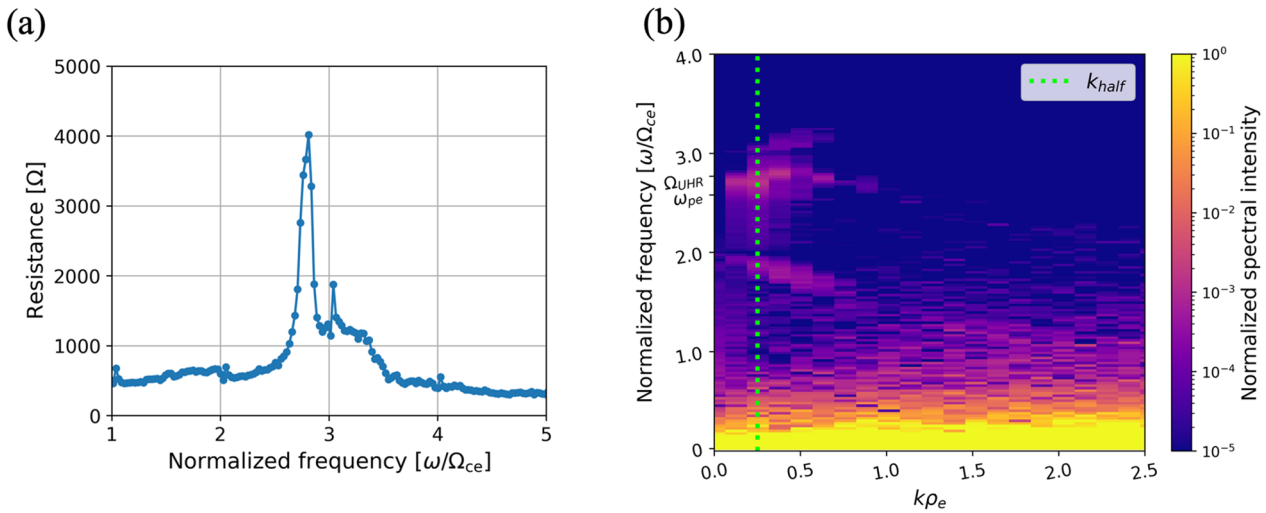

Fig. 7 **a** Comparison of resistance component (real part) of sensor impedance and **b** dispersion relation obtained from simulation for $\theta = 90°$

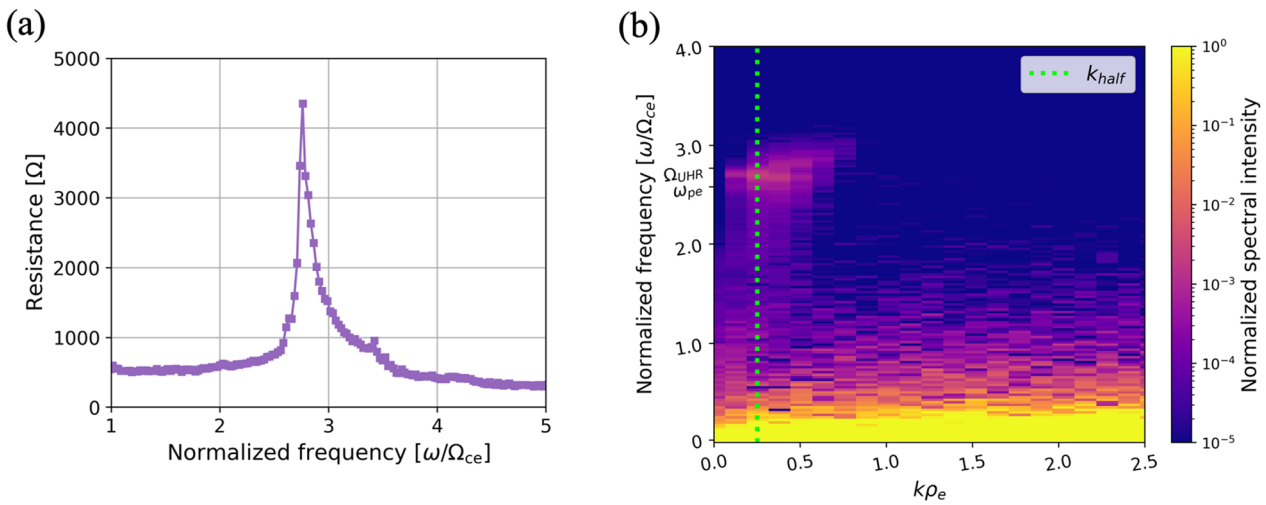

Fig. 8 **a** Comparison of resistance component (real part) of sensor impedance and **b** dispersion relation obtained from simulation for $\theta = 0°$

half-wavelength antenna is uniquely defined by the relation $c = \omega/k$. The resonance in impedance occurs at k_{half}, where $\omega = c/k_{\mathrm{half}}$. On the other hand, in magnetized plasmas, multiple impedance resonances are possible since several wave modes are present at a specific wavenumber. The plasma waves in the simulations are UHR and ECH waves at $\theta = 90°$ and Langmuir waves at $\theta = 0°$. The sensor and these waves are expected to be in resonance at the intersection of these wave branches and at k_{half} in the $\omega - k$ plot.

It can also be seen that the electric field intensity in the $\omega - k$ plot is related to the amplitude of the resistance. In specific, the main resonance peaks are related to the branch in which a large electric field amplitude is present, and moderate peaks appear near the branch with a smaller spectral intensity.

These characteristics are found as well when $\theta = 0°$. Figure 8a and b shows the real part of the sensor impedance and the $\omega - k$ diagram at $\theta = 0°$. The peak of the resistance is located at a frequency where Langmuir branches are presented at $k = k_{\mathrm{half}}$.

Conclusions

We performed three-dimensional PIC simulations to investigate the sensor impedance in magnetized plasmas. We focused on the parametric dependence of sensor impedance at amplitudes of the background magnetic field and the relative angle Θ between the k-vector of plasma wave modes and the background magnetic field. We discussed the dispersion relations to understand the simulation results, which showed notable features in the frequency dependence of the sensor impedance.

The $\omega - k$ plot obtained from the simulation was compared with the sensor impedance. The relation between the absolute value of the amplitude in the $\omega - k$ plot and the impedance peak was confirmed. We conclude that the impedance resonance appears at the frequencies at which the various plasma wave modes intersect in the $\omega - k$ plot and the wavenumber at which the sensor can be regarded as a half-wavelength dipole. As the amplitude of the background magnetic field increases, the resonance frequency also increases with changes in the dispersion relation of the branch connecting to the UHR frequency. One of our main results is that resistance peaks of sensor impedance are related to the electric field intensity in the $\omega - k$ plot.

We showed that sensor impedance can be accurately simulated using the EMSES. The EMSES can perform simulations that take into account the background magnetic field, self-consistent current distribution, and sheath structure, which are difficult to incorporate into numerical calculations. The simulation results enable us to achieve more precise calibration, such as adjusting the calibration table for different observation plasma wave modes. These calibrated characteristics of sensor impedance not only contribute to the accurate calibration of electric field sensors but also facilitate the development of new sensors.

It should be noted that one of the advantages of electromagnetic PIC simulations over numerical calculations is the flexibility of parameters and satellite modeling. In this study, we focus on the simple model including sensor elements in magnetized plasmas. However, in actual satellite observations, there are various structures around electric field sensors, such as sensor booms, satellite bodies and solar panels that might impact sensor impedance. The simulation code used in the present study has the capability to deal with inner structures in the simulation box. Our future studies will introduce more complex models to pursue sensor impedance under realistic situations.

Acknowledgements
The computer simulation was performed on the A-KDK computer system at the Research Institute for Sustainable Humanosphere, Kyoto University.

Author contributions
IF and HK evaluated the reproducibility of plasma waves. SK performed theoretical evaluation of electric field sensor characteristics. HU and YM performed algorithm evaluation. YM evaluated the electric field sensor model. IF and KK performed parameter dependence evaluation. All authors read and approved the final manuscript.

Funding
This work was supported by the Japan Science and Technology Agency Support for Pioneering Research Initiated by the Next Generation program under Grant Number JPMJSP2110. This work was also supported by JSPS KAKENHI under Grant Numbers 21H04520.

Availability of data and materials
The datasets used and analyzed in the current study are available from the corresponding author on reasonable request.

Declarations

Competing interests
There are no competing interests.

Author details
[1]Department of Electrical Engineering, Graduate School of Engineering, Kyoto University, Kyoto University Katsura, Nishigyo-ku, Kyoto, Kyoto, Japan. [2]Graduate School of System Informatics, Kobe University, 1-1 Rokkodai-cho, Nada-ku, Kobe, Hyogo, Japan. [3]Research Institute for Sustainable Humanosphere, Kyoto University, Gokasho, Uji, Kyoto, Japan.

Received: 26 July 2023 Accepted: 6 February 2024
Published online: 01 March 2024

References

Balmain K (1964) The impedance of a short dipole antenna in a magnetoplasma. IEEE Trans Antennas Propag 12(5):605–617

Barrington RE, Belrose JS (1963) Preliminary results from the very-low frequency receiver aboard Canada's alouette satellite. Nature 198(4881):651–656
Bernstein IB (1958) Waves in a plasma in a magnetic field. Phys Rev 109(1):10
Birdsall CK, Langdon AB (2018) Plasma physics via computer simulation. CRC Press, Boca Raton
Hashimoto K, Nagano I, Okada T, Yamamoto M, Kimura I (1991) Antenna vector impedance measurement by the EXOS-D (Akebono) very low frequency plasma wave instrument (VLF). Geophys Res Lett 18(2):313–316
Hunsberger F, Luebbers R, Kunz K (1992) Finite-difference time-domain analysis of gyrotropic media. I. Magnetized plasma. IEEE Trans Antennas Propag 40(12):1489–1495
Luebbers RJ, Hunsberger F, Kunz KS (1991) A frequency-dependent finite-difference time-domain formulation for transient propagation in plasma. IEEE Trans Antennas Propag 39(1):29–34
Matsuda S, Kojima H, KasaharaY KY, Kumamoto A, Fuminori T, Matsuoka A, Miyoshi Y, Shinohara I (2021) Direct antenna impedance measurement for quantitative ac electric field measurement by Arase. J Geophys Res Space Phys 126(6):e2021JA029111
Matsumoto H, Omura Y (1993) Computer space plasma physics, simulation techniques and software. Terra Scientific Publishing Company, Tokyo
Meyer P, Vernet N (1974) Impedance of a short antenna in a warm magneto-plasma. Radio Sci 9(3):409–416
Miyake Y, Usui H (2009) New electromagnetic particle simulation code for the analysis of spacecraft-plasma interactions. Phys Plasm 16(6):062904
Miyake Y, Usui H, Kojima H, Omura Y, Matsumoto H (2008) Electromagnetic particle-in-cell simulation on the impedance of a dipole antenna surrounded by an ion sheath. Radio Sci 43(03):1–14
Schiff ML, Fejer JA (1970) Impedance of antennas in a warm isotropic plasma: a comparison of different models. Radio Sci 5(5):811–819
Spencer E, Patra S, Andriyas T, Swenson C, Ward J, Barjatya A (2008) Electron density and electron neutral collision frequency in the ionosphere using plasma impedance probe measurements. J Geophys Res Space Phys. https://doi.org/10.1029/2007JA013004
Stix TH (1992) Waves in plasmas. American Institute of Physics, New York
Sugiyama H, Singh S, Omura Y, Shoji M, Nunn D, Summers D (2015) Electromagnetic ion cyclotron waves in the Earth's magnetosphere with a Kappamaxwellian particle distribution. J Geophys Res Space Phys 120(10):8426–8439
Tajima T, Lee YC (1981) Absorbing boundary condition and Budden turning point technique for electromagnetic plasma simulations. J Comput Phys 42(2):406–412
Tsutsui M, Nagano I, Kojima H, Hashimoto K, Matsumoto H, Yagitani S, Okada T (1997) Measurements and analysis of antenna impedance aboard the Geotail spacecraft. Radio Sci 32(3):1101–1126
Usui H, Matsumoto H, Yamashita F, Yamamoto A, Omura Y (2004) Antenna analysis in magnetized plasma via particle-in-cell simulation. Adv Space Res 34(11):2433–2436
Wakabayashi M, Ono T (2006) Electron density measurement under the influence of auroral precipitation and electron beam injection during the delta campaign. Earth Planet Space 58(9):1147–1154. https://doi.org/10.1186/BF03352004

Publisher's Note